ELSEVIER

Contents lists available at ScienceDirect

Ceramics International

journal homepage: www.elsevier.com/locate/ceramint



Manganese behavior in hydroxyapatite crystals revealed by X-ray difference Fourier maps



P.H. Oliveira Jr^a, L.A.B. Santana^a, N.S. Ferreira^b, S. Sharifi-Asl^c, T. Shokuhfar^c, R. Shahbazian-Yassar^c, G.M.L. Dalmônico^d, J. Werckmann^d, M. Farina^e, E.A. dos Santos^{a,*}

- ^a Department of Materials Science and Engineering, Federal University of Sergipe, São Cristóvão, 49100-000, Sergipe, Brazil
- ^b Department of Physics, Federal University of Sergipe, São Cristóvão, 49100-000, Sergipe, Brazil
- ^c Department of Mechanical and Industrial Engineering and Department of Bioengineering, University of Illinois at Chicago, Chicago, IL, 60607, United States
- ^d Brazilian Center for Physics Research, Rio de Janeiro, 22290-180, Rio de Janeiro, Brazil
- ^e Institute of Biomedical Sciences, Federal University of Rio de Janeiro, Rio de Janeiro, 21941-902, Brazil

ARTICLE INFO

Keywords: Hydroxyapatite Manganese Manganese oxide Magnetic nanoparticle Crystalline structure

ABSTRACT

The use of magnetic nanoparticles in association with scaffolds is considered an important way to transform typical passive scaffolds into active scaffolds. Manganese can develop magnetic properties in hydroxyapatites, as can iron, copper, cobalt and samarium, but lacks the high toxicity of these latter compounds. Because the magnetic properties exhibited by transition metal-containing hydroxyapatite are entirely dependent on site occupation and on the formation of magnetic oxides under heating, it is extremely important to understand how manganese behaves when inserted into hydroxyapatite. In this paper, we demonstrated by using X-ray difference Fourier maps that the insertion of Mn into the hydroxyapatite structure induces several perturbations in its hexagonal channels, with a preference for occupying Ca(2) sites, particularly when the hydroxyapatite lattice is poorly ordered and has ${\rm CO_3}^{2-}$ inserted at ${\rm PO_4}^{3-}$ sites. When ${\rm CO_3}^{2-}$ is released at high temperature and the structure is better ordered, Ca(1) sites become more susceptible to occupation by Mn atoms, while the occupation of ${\rm PO_4}^{3-}$ sites by ${\rm MnO_4}^{3-}$ is reduced. However, with increasing time and calcination temperature, Mn atoms tend to be released from the hydroxyapatite structure in the form of ${\rm Mn_3O_4}$ nanoparticles through the hydroxyl channels, occupying Ca(2) sites in the final stage of the segregation pathway. These findings are fundamental to the development of new strategies to synthesize active hydroxyapatite-based scaffolds under remote control by a magnetic field.

1. Introduction

Magnetic nanoparticles play an important role in the biomedical engineering field [1,2] and are employed in hyperthermia treatments, nuclear magnetic resonance imaging, controlled drug/gene delivery, and tissue regeneration. The use of magnetic nanoparticles in association with scaffolds has been demonstrated to transform typical passive scaffolds into active scaffolds by two distinct mechanisms remotely activated by a magnetic field [3–6]: a) the diffusion of bioagents induced by mechanical deformations in soft magnetic scaffolds and b) the diffusion of magnetic drug carriers or bioagents induced by a magnetic field gradient generated from a rigid magnetic scaffold. The magnetic guiding process is well known in nanomedicine, but it is little used in scaffold applications for bone graft substitution, especially for controlling the reloading of growth factors, stem cells or other bioagents

after implantation [4,7]. One of the primary problems associated with the biomedical use of magnetic nanoparticles is their toxicity. For this reason, many strategies for developing biocompatible magnetic scaffolds have been studied in biomaterial science [7,8].

Hydroxyapatite is one of the best-known bioceramics used as orthopedic implants and scaffolds in bone tissue engineering [9,10]. Its high biocompatibility and capacity for incorporating different ions into its structure [10,11] make possible, for instance, the production of hydroxyapatite implants and grafts with magnetic properties [8]. Iron, cobalt, manganese, samarium and copper are among the elements used to develop magnetic properties in hydroxyapatite [8,12–14]. Many of these elements present high toxicity and are poorly tolerated in biomedical applications. However, some of these elements have been shown to be capable of inducing osteoblast precursor differentiation through growth factor signaling pathways or stimulating other

E-mail address: euler@ufs.br (E.A. dos Santos).

^{*} Corresponding author.

processes in support of bone tissue growth. For instance, manganese is known to improve hydroxyapatite biocompatibility. Its bivalent ion (Mn²⁺) has been extensively studied in association with calcium phosphates [15–19], and Mn²⁺ is known to be directly involved in bone formation. A deficiency of manganese in the body retards the production of organic extracellular matrices, especially during endochondral ossification [20]. This property is associated with the activation of signaling cascades involved in osteoblast adhesion via integrins [10]. Manganese also has a remarkable effect on osteoblast differentiation, expressed as high osteocalcin production when manganese is inserted into hydroxyapatite [21], and it is associated with moderate antibacterial activity [22,23].

It is highly difficult to stabilize Mn²⁺ ions in the hydroxyapatite structure [24,25]. After thermal treatment at high temperature, Mncontaining hydroxyapatites tend to transform into other phases. The main factors contributing to this instability are the disparate ionic radii and electronegativities of Ca2+ and Mn2+ and the susceptibility of Mn²⁺ ions to oxidation during synthesis or thermal treatment. The typical new phases generated are α -tricalcium phosphate (α -TCP), β tricalcium phosphate (β-TCP), calcium pyrophosphate (CPP) and manganese oxides [15,26,27], most of which exhibit lower biocompatibility than hydroxyapatite. However, one of the oxides that can be generated in this process is Mn₃O₄. This oxide is insoluble in physiological conditions [28], and because of its magnetic properties [29], it can be considered a promising material to produce magnetically active hydroxyapatite-based composite scaffolds. Since the magnetic properties exhibited by transition metal-containing hydroxyapatite and its oxides are dependent on the size, shape, and architecture of the particles [30], including the occupation of hydroxyapatite sites [31,32], it is extremely important to understand how manganese behaves when inserted into a hydroxyapatite phase.

The objective of this work was to study the accommodation of manganese into the hydroxyapatite lattice and to describe the segregation pathway involved in the formation of $\rm Mn_3O_4$ nanoparticles during thermal treatment by using wavelength-dispersive X-ray fluorescence (WDXRF), Rietveld refinement of X-ray diffraction (XRD) data, Fourier transform infrared spectroscopy (FTIR), X-ray photoelectron spectroscopy (XPS), and scanning transmission electron microscopy (STEM) coupled with energy-dispersive X-ray spectroscopy (EDS).

2. Materials and methods

2.1. Hydroxyapatite synthesis

2.1.1. Pure hydroxyapatite

Pure hydroxyapatite powder was synthesized by a wet precipitation method through an acid-base reaction, as described below (Eq. (1)):

$$6H_3PO_4 + 10Ca(OH)_2 \rightarrow Ca_{10}(PO_4)_6(OH)_2 + 18H_2O$$
 (1)

A solution of 0.334 mol L^{-1} calcium hydroxide was dripped (4.0 mL min $^{-1}$) into phosphoric acid (0.220 mol L^{-1}) under stirring at 60 °C. The pH was maintained at 10 with the addition of KOH. After the complete addition of the reactants, the suspension was aged for 20 min under reflux in a microwave oven operating at 700 W and 2.5 GHz to avoid crystal growth, keeping the precipitate particles in the nanoscale state. The precipitate was filtered, washed in distilled water until the supernatant was neutral (pH = 7), and air-dried at 120 °C for 24 h. Finally, the residue was ground using an agate mortar and sieved (180 mesh). All reagents were of high purity (\geq 98%) and were purchased from Sigma-Aldrich.

2.1.2. Mn-containing hydroxyapatites

Mn-containing hydroxyapatite powders were obtained using the same procedure described above (item 2.1.1). The amount of Mn^{2+} ions used was calculated to produce $\mathrm{Mn/(Mn} + \mathrm{Ca})$ atomic ratios of 5, 10, 15 and 20%. Manganese nitrate tetrahydrate was added to the

phosphoric acid to prevent the oxidation of manganese(II) ions to higher valence states.

2.2. Thermal treatment

Portions of the obtained powders were subjected to heat treatment (calcination) at $1000\,^{\circ}\text{C}$ for 2 h under atmospheric conditions at a heating rate of approximately $2\,^{\circ}\text{C/min}$. The powders before and after calcination were termed the as-synthesized and calcined powders, respectively. To study the segregation of Mn_3O_4 , the powder containing 4.9% Mn was also calcined at 400, 600, 800 and 1000 $^{\circ}\text{C}$ for 5 min (heating rate of $2\,^{\circ}\text{C/min}$).

2.3. Chemical composition

The elements present in each sample and their concentrations were measured using wavelength-dispersive X-ray fluorescence (WDXRF) in a Bruker S8-Tiger 4 kW spectrometer. The obtained powders were directly analyzed under a He atmosphere. A calibration curve was established using standard hydroxyapatite (Ca/P = 1.67) powder homogenously ground in a ball mill apparatus for 30 min at 350 rpm with different concentrations of standard MnO powder.

2.4. Structural characterization

2.4.1. X-ray diffraction

The as-synthesized and calcined samples were analyzed by XRD. The diffraction patterns were collected in an Empyrean PANalytical diffractometer using CuK_{α} radiation (Ni filter) at 40 kV and 40 mA. The data were recorded from $2\theta=10^{\circ}$ to 60° with a step size of 0.013° and a collection time of 2 s. The crystalline structure was solved and refined using the Rietveld refinement method as implemented in Fullprof software [33] (version 07/2017). The refinement was conducted from previously known standard structures obtained from the Inorganic Crystal Structure Database (ICSD): pure calcium apatite $Ca_{10}(PO_4)_6(OH)_2$ (ICSD n° 151414), pure manganese oxide Mn_3O_4 (ICSD n° 68174), and pure β -tricalcium phosphate $Ca_3(PO_4)_2$ (ICSD n° 410782).

The background, scale factor, specimen displacement, cell unit parameters (a and c), peak profile (Caglioti parameters, asymmetry and peak shape), preferred orientation, and site occupation were refined to calculate the cell parameters, crystallite sizes, microstrains and amounts of phases. These same parameters were refined to calculate the difference Fourier maps (Fobs - Fcal), except for the site occupation. Our intention was to identify the differences between the observed and calculated X-ray diffraction patterns induced by Mn atoms. The maps were superposed with the hydroxyapatite cell unit structure in 2D and 3D views using Vesta software [34]. The average crystallite size and lattice strain were estimated from the Rietveld refinement considering the changes in the Caglioti parameters (U and V) between a standard instrument profile and the samples.

2.4.2. Fourier transform infrared spectroscopy

The as-synthesized and calcined samples were analyzed by FTIR. The analyses were conducted in absorbance mode from 4000 to 400 cm $^{-1}$ (step size of 1 cm $^{-1}$) using a Varian (640-IR) spectrometer. The region between 500 and 650 cm $^{-1}$ was used to observe the behavior of HPO $_{\rm 4}^{2-}$, PO $_{\rm 4}^{3-}$ and OH $^{-}$ groups, and the region from 850-890 cm $^{-1}$ was used to follow the insertion of CO $_{\rm 3}^{2-}$ groups into the PO $_{\rm 4}^{3-}$ and OH $^{-}$ sites of the hydroxyapatite phase. The absorption band positions were based on the previous work of Eichert et al. [35].

2.4.3. Transmission electron microscopy

The sample containing 4.9 mol % Mn after calcination was characterized by scanning transmission electron microscopy (STEM) in a JEOL JEM-2100F electron microscope (Brazilian Center for Research in

Physics - Brazil) and an aberration-corrected JEOL JEM-ARM200CF electron microscope (University of Illinois at Chicago - USA), both equipped with a field emission gun (FEG) and operated at 200 kV. The elemental composition in different regions of the crystal agglomerates was obtained by energy-dispersive X-ray spectroscopy (EDS).

2.4.4. X-ray photoelectron spectroscopy

As-synthesized samples containing 4.9% Mn and those calcined at 800 °C for 5 min and at 1000 °C for 2 h were analyzed by X-ray photoelectron spectroscopy (XPS). The analyses were performed in a Thermo Scientific ESCALab 250Xi spectrometer using a monochromatic Al Ka X-ray source. The binding energy was calibrated with C 1s (284.8 eV) [36,37]. The Mn 2p_{3/2} spectra were deconvoluted after baseline subtraction to calculate the relative area under the curves corresponding to Mn(II) (641.4 eV: MnO), Mn(III) (642.1 eV: Mn₂O₃) and Mn(IV) (642.9 eV: MnO₂) oxidation states [38-42].

3. Results

3.1. Elemental composition

The Ca concentration decreased markedly with increasing Mn, while the amount of P decreased slightly (Fig. 1). The measured Ca/P ratios were all below the stoichiometric value of 1.67, suggesting the formation of a Ca-deficient hydroxyapatite. Furthermore, the (Ca + Mn)/P ratio was higher than 1.67 for all the samples containing Mn, indicating an excess of cations or a lack of PO₄³⁻ groups. The relative concentration of Mn, i.e., the Mn/(Mn + Ca) ratio, observed (Obs) for the obtained samples was slightly different from that calculated (Cal) for the synthesis, especially for the highest Mn concentrations.

3.2. Phase composition

Ca/P

XRD analyses demonstrated the formation of a hydroxyapatite phase in all samples (Fig. 2a). No other phase was observed, suggesting that the Mn atomic content determined by WDXRF was inserted into the hydroxyapatite structure. This hypothesis is further supported because the increase in Mn concentration led to remarkable peak broadening, which indicates higher lattice disorder. This disorder is reflected in the phase transformations observed after calcination at 1000 °C for 2 h. Only the sample without Mn (0.0% Mn) was not transformed after calcination. For all the Mn-containing samples, the

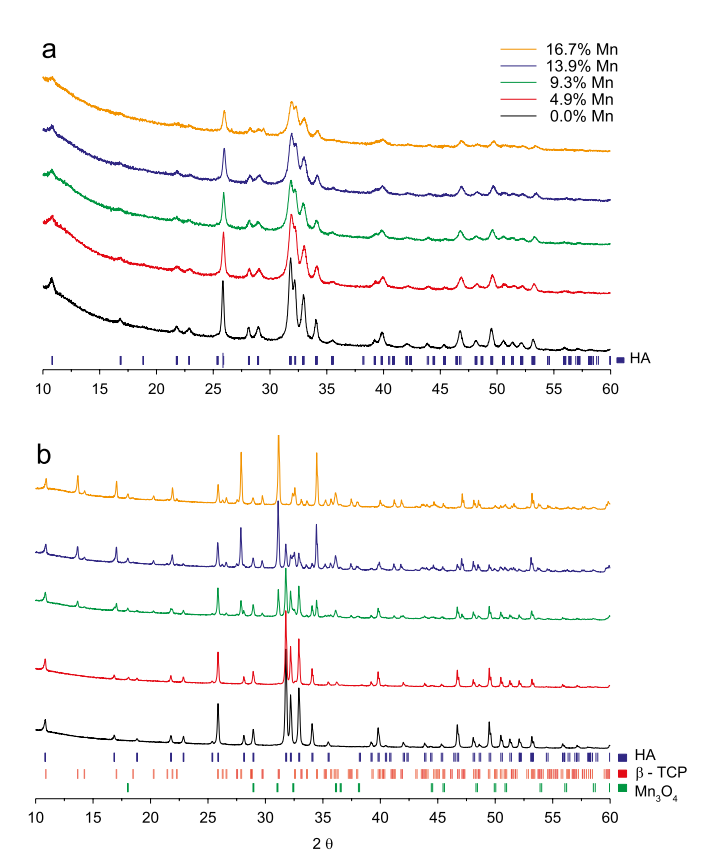


Fig. 2. X-ray diffraction (XRD) patterns obtained for samples with different Mn concentrations (measured by WDXRF) before (a) and after (b) calcination at 1000 °C for 2 h. The standard diffraction patterns of each identified phase, namely, hydroxyapatite (HA), β-tricalcium phosphate (β-TCP) and manganese oxide (Mn₃O₄), are indicated in the graphic (Supplementary data: Figs. S1-S10).

transformation produced manganese oxide (Mn₃O₄). Above 4.9% Mn, β-tricalcium phosphate (β-TCP) was also verified (Figs. 2b and 3). The amounts of both β-TCP and Mn₃O₄ produced during calcination increased with Mn concentration. For the highest concentration of Mn (16.7% Mn), all hydroxyapatite was transformed into β-TCP and Mn_3O_4 .

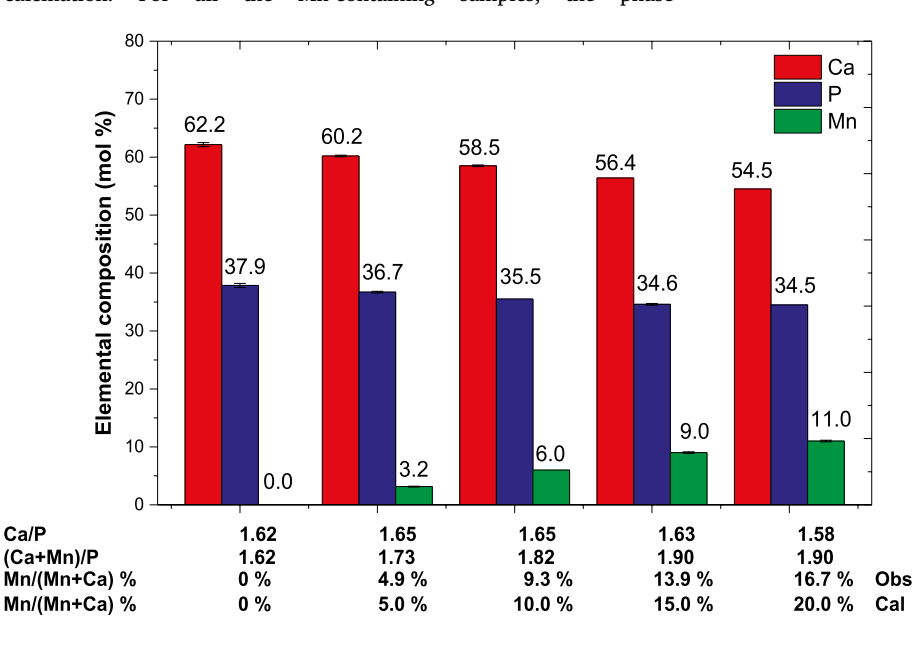


Fig. 1. Relative amounts of Ca, P and Mn (mol %) measured by wavelength-dispersive X-ray fluorescence (WDXRF) as a function of the calculated (Cal) Mn/(Mn + Ca) ratio used in the synthesis of five different samples. The Ca/P, (Ca + Mn)/P and Mn/ (Mn + Ca) ratios measured by WDXRF (Obs) are provided for each condition.

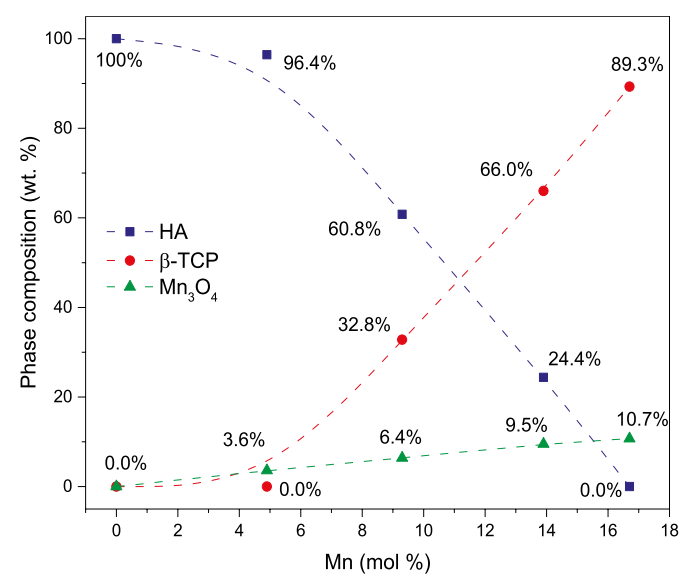


Fig. 3. Phase composition obtained from Rietveld refinement of samples with different Mn concentrations (measured by WDXRF) after calcination at 1000 °C for 2 h (Supplementary data: Figs. S6–S10).

Scanning transmission electron microscopy and energy-dispersive X-ray spectroscopy (STEM/EDS) analysis of the samples containing 4.9% Mn after calcination for 2 h showed the formation of $\rm Mn_3O_4$ nanocrystals (Fig. 4), caused by Mn segregation from the as-synthesized Mn-containing hydroxyapatite. The amount of Mn remaining in the hydroxyapatite phase

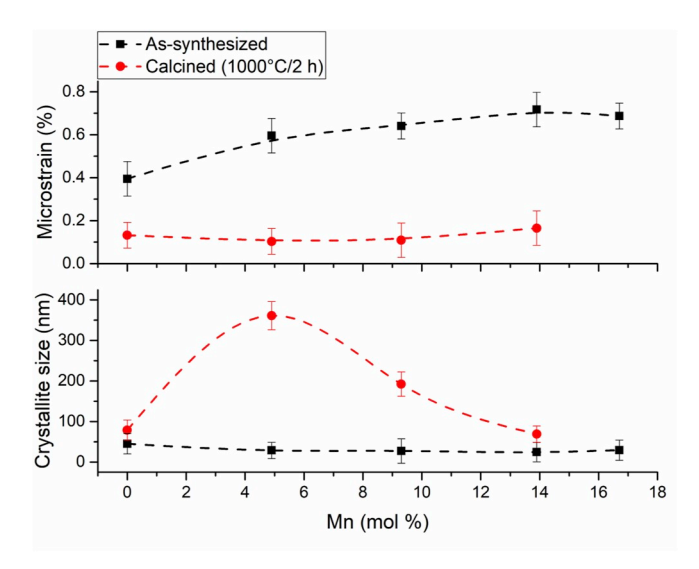


Fig. 5. Microstrains and average crystallite sizes calculated from the hydroxyapatite phase via Rietveld refinement for increasing concentrations of Mn (measured by WDXRF) (Supplementary data: Figs. S1–S10).

was measured by EDS in different regions of the hydroxyapatite particles far from the large $\rm Mn_3O_4$ particles. The EDS maps showed a heterogeneous distribution of Mn throughout the hydroxyapatite crystals, suggesting that the segregation event was not completed after 2 h of calcination. The relative amounts of Mn, i.e., Mn/(Mn + Ca), in two distinct areas, as detailed in Fig. 4, were 0.34 and 0.70 at. %.

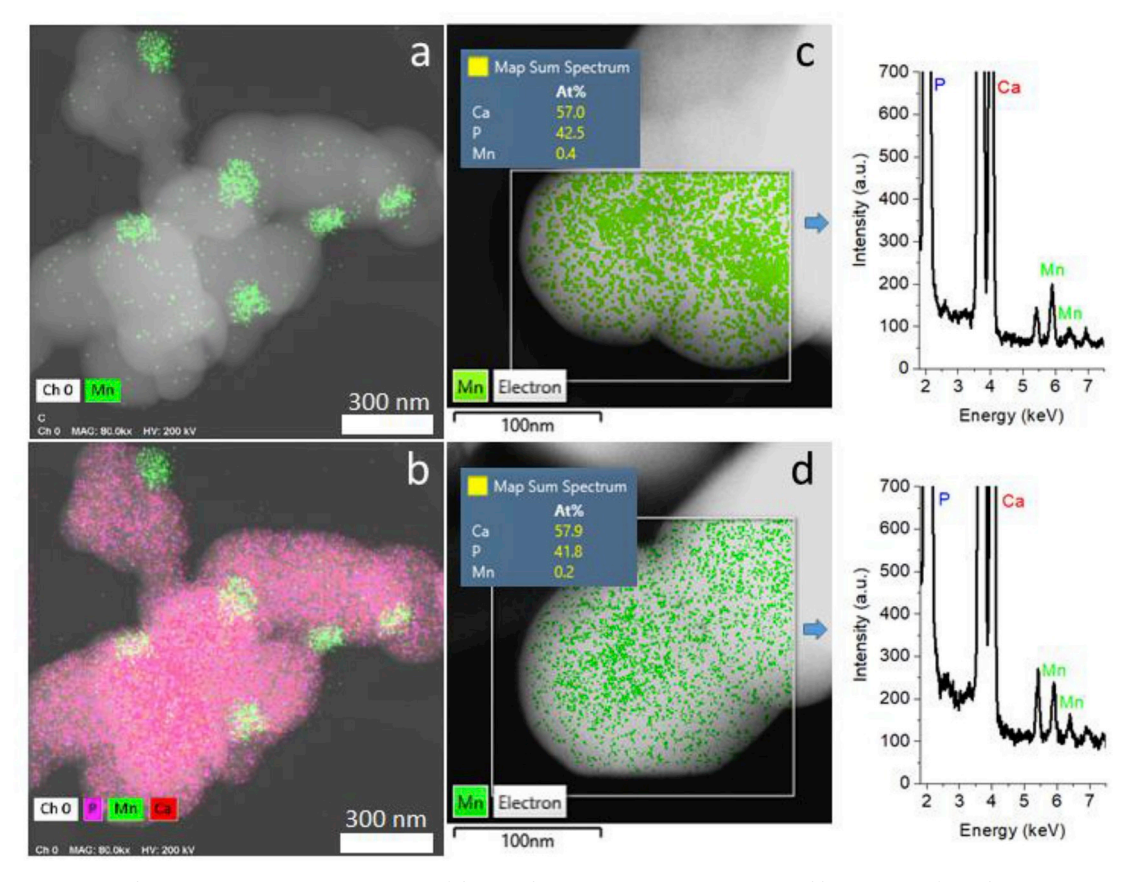


Fig. 4. Scanning transmission electron microscopy (STEM) images of the sample containing 4.9% Mn (measured by WDXRF) after calcination at 1000 °C for 2 h. The energy-dispersive X-ray spectroscopy (EDS) elemental maps show the localization of the Mn_3O_4 nanocrystals segregated from the Mn-containing hydroxyapatite phase after calcination (a, b). The detailed EDS maps acquired in regions far from the Mn_3O_4 nanocrystals (c, d) show the heterogeneous distribution of Mn throughout the hydroxyapatite crystals and their respective spectra.

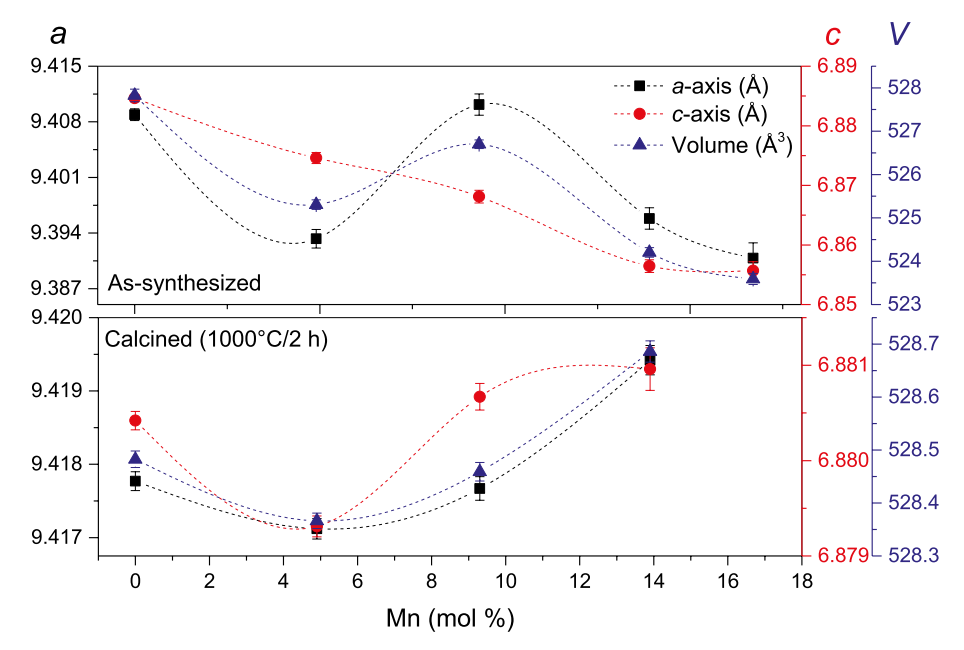


Fig. 6. Lattice parameters (*a*- and *c*-axis) and cell unit volume (*V*) calculated from the hydroxyapatite phase via Rietveld refinement for increasing concentrations of Mn (measured by WDXRF) (Supplementary data: Figs. S1–S10).

3.3. Crystalline structure

The microstrain and average crystallite size of the hydroxyapatite phase before and after calcination were estimated from the Rietveld refinement (Fig. 5). The insertion of Mn increased the microstrain of the as-synthesized hydroxyapatite samples. However, calcination promoted lattice relaxation, as the microstrain was remarkably reduced. Moreover, the average crystallite size measured before calcination was lower than 50 nm, regardless of the Mn concentration. Calcination promoted an increase in the average crystallite size, especially in the samples containing 4.9% Mn. Because the hydroxyapatite phase was no longer observed in the samples at 16.7% Mn (Fig. 3), the microstrain and average crystallite size were not calculated for this concentration.

In general, the hydroxyapatite lattice parameters measured before calcination decreased with increasing Mn (Fig. 6). The c-axis was notably more sensitive to the amount of Mn, presenting an almost linear decrease with the Mn concentration. After calcination, the presence of 4.9% Mn also decreased the lattice parameters relative to those of pure hydroxyapatite. However, at 9.3% Mn, the lattice parameters increased again, reaching higher values than those observed for pure hydroxyapatite. At 16.9% Mn, only the β -TCP phase was observed, which impaired the calculation of the hydroxyapatite lattice parameters at this concentration.

3.4. Occupation of HA sites

3.4.1. Molecular groups in hydroxyapatite

Fourier transform infrared spectroscopy (FTIR) analyses showed that the absorption bands at 632 cm $^{-1}$ associated with the O–H translational mode (libration) of hydroxyl groups ($\nu_L \rm OH^-$) decreased with increasing concentrations of Mn, especially for the as-synthesized samples (Fig. 7). The absorption bands related to the PO_4 3 – groups in hydroxyapatite had three ν_4 asymmetric bending modes for O–P–O bonds at 565, 571, and 602 cm $^{-1}$. Broadening and intensity reduction were observed in these absorption bands at increasing concentrations of Mn. After calcination, typical PO_4 3 – absorption bands from β -TCP were verified at 551 and 603 cm $^{-1}$, especially for the samples with 13.9 and 16.7% Mn. Characteristic absorption bands of HPO_4 2 – groups were observed as shoulders at approximately 551 cm $^{-1}$ for the as-synthesized samples and decreased with Mn concentration.

Absorption bands for $\mathrm{CO_3}^{2-}$ groups were verified, especially on the as-synthesized samples. At 870 cm $^{-1}$, the characteristic ν_2 out-of-plane bending vibration of O–C–O groups indicated the occupation of $\mathrm{PO_4}^{3-}$ sites (B-type substitution). These bands were overlapped by another at 880 cm $^{-1}$, which was associated with the occupation of OH^- sites (A-type substitution), indicating the presence of both substitutions. The insertion of Mn simultaneously shifted the band to the region of B-type $\mathrm{CO_3}^{2-}$ groups and exhibited a broadening effect. After calcination, only the pure hydroxyapatite sample retained absorption bands in that region.

3.4.2. Difference Fourier maps

Difference Fourier maps were calculated from the Rietveld refinement to infer the main perturbations that occurred in the Ca^{2^+} , PO_4^{3^-} and OH^- sites of the hydroxyapatite phase upon the insertion of Mn atoms. The maps were calculated only for the samples with 0.0 and 4.9% Mn because β -TCP was absent in these samples after calcination.

For the as-synthesized hydroxyapatite sample without Mn (0.0% Mn), the Ca(2) sites (Wyckoff position 4f) presented a negative scattering density residue, suggesting the presence of Ca^{2+} vacancies (Fig. 8). The regions close to the P(1) sites (Wyckoff position 6 h) had a positive scattering residue, especially between the P(1) and Ca(2) sites (Wyckoff position 6 h) in the neighborhood of PO_4^{3-} groups, clearly demonstrating the presence of substitutional molecules or rotation of the original PO_4^{3-} groups. The regions of O(4) oxygens from hydroxyl groups (between two adjacent H(1) atoms), both at Wyckoff position 4e, were slightly positive. The insertion of 4.9% Mn into the hydroxyapatite structure strongly decreased the negativity of the Ca(1) sites, while a positive scattering residue was retained between Ca(2) and PO_4^{3-} sites. Moreover, the hydroxyl sites become slightly negative.

After calcination, the Ca(2) sites of the hydroxyapatite without Mn became less perturbed than before calcination, while the column between two Ca(1) sites (in the middle of the three O(1)/O(2) sites) along the [0 0 1] direction became markedly negative. P(1) sites became positive, while OH $^-$ regions became negative. The presence of 4.9% Mn caused a strong perturbation in the hydroxyl channel. Strong positive scattering residue regions close to the Ca(2) sites were observed with a very negative ring around the H(1) site. P(1) sites were still positive, but perturbations in the Ca(1) sites were no longer observed.

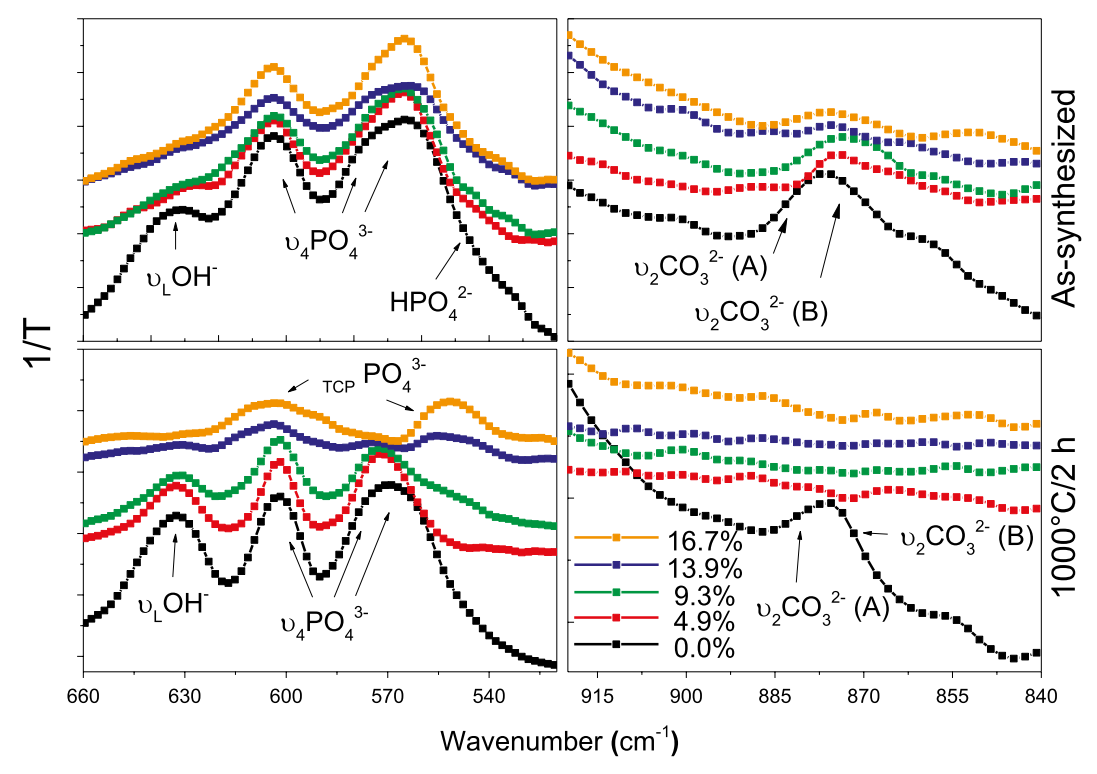


Fig. 7. FTIR spectra near the $\nu_4 PO_4^{~3}$ –, $\nu_L OH^-$, $HPO_4^{~2}$ and $\nu_2 CO_3^{~2}$ absorption bands obtained for samples with different Mn concentrations (measured by WDXRF) before (above) and after (below) calcination at 1000 °C for 2 h.

3.4.3. XPS

The Mn oxidation states in the samples containing 4.9% Mn were estimated by analyzing the changes in the Mn $2p_{3/2}$ XPS spectra (Fig. 11) before and after heat treatment at 800 °C/5 min and 1000 °C for 2 h. The deconvoluted curves showed a low amount of Mn^{2+} but a high amount of oxidized Mn forms, notably Mn^{3+} and Mn^{4+} , in the as-

synthesized samples. After calcination at 800 °C/5 min, the amount of ${\rm Mn}^{3+}$ increased, while the amount of ${\rm Mn}^{4+}$ decreased, and the amount of ${\rm Mn}^{2+}$ remained the same. However, after 1000 °C for 2 h, the whole curve shifted to a lower binding energy, which increased the relative amount of ${\rm Mn}^{2+}$ ions.

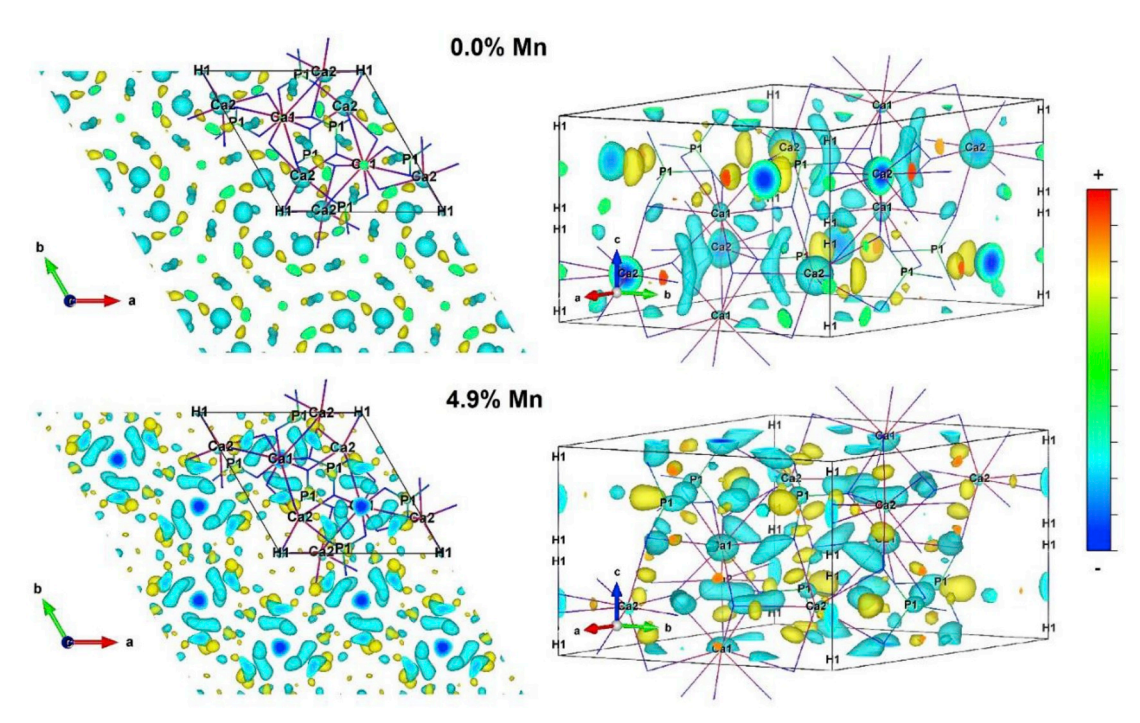


Fig. 8. 3D difference Fourier maps $(F_{obs} - F_{cal})$ obtained for hydroxyapatite phases containing 0.0 (Supplementary data: Fig. S11) and 4.9 (Supplementary data: Fig. S13) mol % Mn (measured by WDXRF) before calcination (as-synthesized powder). 2D images of 4 cell units of hydroxyapatite are observed along the [0 0 1] direction (left). 3D images of cell units of hydroxyapatite show in detail the perturbations around the Ca(1), Ca(2), P(1) and H(1) sites (right).

4. Discussion

4.1. As-synthesized hydroxyapatite structure

XRD analysis of the as-synthesized samples confirmed the presence of a single hydroxyapatite phase (Fig. 2). Furthermore, elemental analysis by WDXRF showed that this hydroxyapatite phase had a Ca/P ratio below the stoichiometric value of 1.67 (Fig. 1), which was characteristic of a Ca-deficient hydroxyapatite. Such deficiency is usually caused by the entry of additional acidic phosphates, such as $\mathrm{HPO_4}^{2-}$ ions, into the hydroxyapatite structure during synthesis. The insertion of such ions generates Ca^{2+} (V_{Ca}) and OH^- (V_{OH}) vacancies, which can be represented in Kröger-Vink notation [43–45] (Eq. (2)):

$$(Ca)_{Ca}^{x} + (PO_{4})_{PO_{4}}^{x} + (OH)_{OH}^{x} + HPO_{4(aq)}^{2-} \rightarrow (HPO_{4})_{PO_{4}}^{*} + V_{Ca}^{'} + V_{OH}^{*} + PO_{4(aq)}^{3-}$$
(2)

According to the acid-base equilibrium observed for orthophosphate anions (Eq. (3)), for the pH conditions used in this work (pH = 10), the protonated $\mathrm{HPO_4}^{2-}$ species tend to predominate in the reaction medium [31,32], facilitating $\mathrm{HPO_4}^{2-}$ entry into the hydroxyapatite structure [46,47]:

$$H_3PO_4$$
 $K_I = 7.5 \times 10^{-3}$ $H_2PO_4^ K_{II} = 6.2 \times 10^{-8}$ HPO_4^{2-} $K_{III} = 1.7 \times 10^{-12}$ PO_4^{3-} (3)

FTIR analysis demonstrated the presence of HPO_4^{2-} in the samples (Fig. 7). The difference Fourier maps also showed negative scattering at Ca(2) sites for the as-synthesized samples without Mn (Fig. 8), which reinforced the presence of Ca^{2+} vacancies in the synthesized hydroxyapatite. The presence of CO_3^{2-} was also detected in both A- and B-type substitutions by FTIR (Fig. 7). The entry of CO_3^{2-} into PO_4^{3-} (B-type) and OH^- (A-type) sites is described by the following mechanisms (Kröger-Vink notation) [43,44] (Eqs. (4) and (5)):

$$(PO_4)_{PO_4}^x + (OH)_{OH}^x + CO_{3(aq)}^{2-} \rightarrow (CO_3)_{PO_4}^* + (CO_3)_{OH}' + PO_{4(aq)}^{3-} + OH_{(aq)}^{-}$$

$$2(OH)_{OH}^{x} + CO_{3(aq)}^{2-} \rightarrow (CO_{3})_{i}' + 2V_{OH}^{*} + 2OH_{(aq)}^{-}$$
 (5)

According to this mechanism, a probable chemical formula for the as-synthesized hydroxyapatite phase without Mn could be represented as follows [48] (Eq. (6)):

$$Ca_{10-(x+y)}(V_{Ca})_{x+y}[(PO_4)_{6-(x+y)}(HPO_4)_x(CO_3)_y](OH)_{2-(x+y)+2z}(CO_3)_z(V_{OH})_{x+y+2z}$$
(6)

The presence of the $\mathrm{HPO_4}^{2^-}$ and $\mathrm{CO_3}^{2^-}$ species in the $\mathrm{PO_4}^{3^-}$ sites was suggested not only by the FTIR results but also by the difference Fourier maps, which indicated pronounced perturbations (positive scattering residues) around the $\mathrm{PO_4}^{3^-}$ sites. Although carbon (C: $17.86 \times 10^{-6} \, \text{Å}^{-2}$) and phosphorus (P: $15.26 \times 10^{-6} \, \text{Å}^{-2}$) have similar X-ray scattering length densities, the geometries of $\mathrm{CO_3}^{2^-}$ and $\mathrm{PO_4}^{3^-}$ ions are different, which generates perturbations around P(1) sites. Moreover, the positive scattering observed at O(4) sites (belonging to hydroxyl groups) suggests occupation by $\mathrm{CO_3}^{2^-}$. When hydroxyl groups are replaced by $\mathrm{CO_3}^{2^-}$, the presence of carbon, which has a higher scattering length density than oxygen (O: $9.74 \times 10^{-6} \, \text{Å}^{-2}$), tends to increase the electron density in the O(4) region, as observed in the Fourier maps. Thus, a calcium-deficient carbonated hydroxyapatite very similar to that observed in the mineral phase of bones was synthesized [35,49].

4.2. Effect of Mn on the structure of as-synthesized hydroxyapatite

The insertion of Mn into the hydroxyapatite structure was

confirmed since the WDXRF analyses demonstrated the presence of Mn in the samples (Fig. 1), and a single phase of hydroxyapatite was identified by XRD (Fig. 2a) for all as-synthesized samples. Pronounced atomic disorder was observed for increasing concentrations of Mn, which was evidenced by the broadening of the main X-ray diffraction peaks. This disorder was accompanied by a gradual increase in microstrains and the formation of small crystallite sizes (smaller than 50 nm for all as-synthesized samples) (Fig. 5). Furthermore, a gradual decrease in lattice parameters was observed when the Mn concentration increased, especially for the c-axis. Mayer et al. [27] did not observe any apparent effect of Mn on the hydroxyapatite lattice for concentrations between 0.14 and 1.08 wt %. The results of Paluszkiewicz et al. [26] showed a slight decrease in the c-axis for hydroxyapatites containing between 0 and 5 wt% Mn after calcination at 800 °C. They also showed an evident increase in cell unit volume, especially for samples calcined at 1250 °C. They attributed this increase to the insertion of Mn into PO₄³⁻ sites in the form of MnO₄³⁻. While Ca²⁺ has an ionic radius of approximately 1.00 Å in octahedral coordination, Mn^{2+} may have ionic radii as distinct as 0.67 Å and 0.83 Å for the same coordination number in low- and high-spin bonds [25], respectively. Mn3+ presents even smaller ionic radii for the same coordination number (0.58 Å and 0.64 Å in low- and high-spin bonds, respectively). Therefore, it is expected that the insertion of Mn into a calcium phosphate structure induces a decrease in the cell unit parameters. Indeed, LeGeros et al. [50] demonstrated that Mn tends to decrease the cell unit volume of apatites. Other works [15,51] have also demonstrated that the insertion of Mn into the β-TCP structure leads to a decrease in the lattice parameters. Kandori et al. [52,53] synthesized a series of Mn-containing hydroxyapatites under similar conditions to those used in our work and found a decrease in the lattice parameters with Mn concentration. Their results also demonstrated that the decrease in the c-axis was much more pronounced than that observed for the *a*-axis, exactly as observed here.

Other remarkable effects of Mn insertion into the hydroxyapatite phase were evident in the FTIR absorption bands for CO_3^{2-} and OH^{-} groups (Fig. 7). The $\nu_L OH^-$ absorption mode became less intense with the insertion of Mn, indicating substantial perturbation in the hydroxyl channels. Indeed, the previous positive X-ray scattering residue observed between adjacent H(1) sites in the difference Fourier maps became negative after the insertion of 4.9% Mn (Fig. 8). Furthermore, the ν_2 out-of-plane bending vibration of O-C-O groups in ${\rm CO_3}^{2-}$ diminished and shifted to the B-type substitution region. The positive scattering residue observed in the OH⁻ positions before the introduction of Mn ions was attributed to the presence of CO_3^{2-} . One can assume that when Mn is inserted, CO_3^{2-} prefers to occupy the PO_4^{3-} sites, generating hydroxyl vacancies (V_{OH}) , which are expressed as negative scattering residues in the Fourier maps. Considering the negative scattering observed in the Ca(1) sites after the insertion of 4.9 mol % Mn and the predominance of positive regions between Ca(2) and PO_4^{3} sites, it is possible to hypothesize that the Mn atoms were preferentially accommodated in the Ca(2) sites, impairing the insertion of CO₃²⁻ (a much larger molecule) in the OH - position.

The mechanism by which Mn atoms are inserted into hydroxyapatites is not yet clearly understood, especially the occupation of the hydroxyapatite sites [25,27,54]. One of the most detailed descriptions of the occupation of the Ca sites by Mn in apatites was given by Suitch et al. [55]. By using neutron diffraction, Rietveld refinement and infrared (IR) spectroscopy analyses, they observed that Mn had a preference for Ca(1) sites in synthetic fluorapatites calcined at 900 °C. Later, Hughes et al. [56] also noted the preference of Mn for Ca(1) sites in natural apatites, and this result was accompanied by other studies [57]. However, in all cases, the authors analyzed the behavior of Mn in fluorapatites with complex elemental compositions and not in hydroxyapatites. For instance, the composition of the natural fluorapatite Hughes et al. [56] was

 $(Ca_{8.81}Mn_{1.00}Fe_{0.10}Na_{0.07}Ce_{0.02})_{10}P_6O_{24}(F_{1.48}OH_{0.52})$. The presence of other elements and fluoro groups instead of hydroxyl groups in the hexagonal channels might alter the apatite behavior [57]. Consequently, the doping mechanisms and accommodation of specific atoms into the apatite structure can also be changed, especially in simultaneously substituted hydroxyapatites [24] or when other Mn oxidation states could be involved.

The XPS results showed that the amount of Mn(II) in the as-synthesized samples was smaller than the amounts of Mn(III) and Mn(IV) (Fig. 11). This is strong evidence that Mn²⁺ ions were oxidized during the synthesis procedure and inserted into the apatite lattice under higher oxidation states. This evidence is even stronger if we consider the following aspects:

- a) The color of the as-synthesized samples containing 4.9% Mn was green-gray, in contrast to the white color observed for the samples without Mn. In general, the development of color in Mn-containing apatites involves higher Mn oxidation states than Mn(II) [27,58].
- b) The amount of Ca found in the samples with increasing concentrations of Mn decreased at a smaller rate than the increase in Mn, as shown by WDXRF (Fig. 1). At the same time, the amount of P decreased when Mn was added, which means that Mn was likely to replace not only Ca but also P sites.

In recent papers, Kandori et al. [52] and Zou et al. [38] noticed the presence of Mn(III) and Mn(IV) species in a hydroxyapatite synthesized under similar conditions to those used in our work. Kandori et al. [52] explained the presence of these Mn oxidation states by the alkaline conditions and the availability of oxygen in the synthesis reaction. Under these conditions, $\mathrm{Mn^{2+}}$ ions can be easily oxidized, generating ions with higher valences. Even though the $\mathrm{Mn^{2+}}$ ions were previously dissolved into the $\mathrm{H_3PO_4}$ solution to avoid oxidation, the reaction with $\mathrm{Ca(OH)_2}$ occurred at a high pH (pH = 10), as described in item 2.1.1. Using EPR spectroscopy, Mayer et al. [27] observed only Mn(II) in their as-synthesized hydroxyapatite samples. However, in this case, the synthesis occurred in acidic conditions, which are likely to avoid the oxidation of $\mathrm{Mn^{2+}}$ during apatite precipitation.

Therefore, our results strongly indicated that the accommodation of Mn atoms into an as-synthesized calcium-deficient hydroxyapatite containing ${\rm CO_3}^{2-}$ with low crystallinity led to several perturbations around the Ca(2) and OH sites, suggesting the occupation of Ca(2) sites not only by Mn2+ ions but also by Mnn+ species in higher oxidation states. In addition, the perturbations observed around the PO₄³⁻ sites (Fig. 8) suggested that Mn could also replace these groups in the form of oxo species (MnO_4^{n-}), as previously suggested by Mayer et al. [27]. In MnO_4^{3-} , MnO_4^{2-} , and MnO_4^{-} ions, Mn atoms assume the oxidation states V, VI and VII, respectively. These oxidation states can be observed by XPS at higher binding energies than that of Mn(IV) (642.9 eV), namely, 643.5 eV Mn(VI), 644.4 eV Mn(VI) and 645.5 eV Mn(VII), because the increasing oxidation states lead to a linear increase in the Mn $2p_{3/2}$ binding energy [41,42] (Supplementary data: Fig. S19). Because the Mn $2p_{3/2}$ XPS curves obtained from our samples were significantly spread toward higher binding energies, the insertion of MnO₄³⁻ ions into the apatite lattice must indeed be considered. In particular, MnO₄³⁻ species are known to be stabilized in several alkaline earth phosphate lattices, such as apatites [58,59]. Of course, the insertion of all these Mn species might generate a very unstable apatite structure, reflected by increased microstrain and the broadening of XRD peaks, as observed in Figs. 5 and 2a, respectively. The next question is how this apatite structure and especially the Mn atoms respond to thermal treatment at high temperature.

4.3. Mn segregation pathway after heating

After calcination at 1000 °C for 2 h, the hydroxyapatite phase became much more ordered (high crystallinity), as clearly observed by a) the increase in X-ray diffraction peak intensities (Fig. 2b), b) the decrease in microstrain (Fig. 5), c) the increase in crystallite size (Fig. 5), and d) the better definition of the OH^- and PO_4^{3-} absorption bands (Fig. 7).

The insertion of 4.9 mol % Mn did not induce the formation of β-TCP during calcination (Figs. 2-3). However, the formation of 3.6 wt % Mn₃O₄ was observed, which means that some of the Mn atoms inserted into the as-synthesized hydroxyapatite phase were segregated (Fig. 4). This segregation relaxed the lattice, decreasing the microstrain (Fig. 5) after calcination, demonstrating the great difficulty of accommodating Mn atoms in an ordered hydroxyapatite structure. However, the XRD and WDXRD results suggested that some of the Mn atoms remained in the hydroxyapatite structure. The relative weight of Mn₃O₄ formed after calcination and estimated by Rietveld refinement gives a Mn/ (Mn + Ca) ratio of 4.6 mol %, assuming the coexistence of $Ca_{10}(PO_4)_6(OH)_2$ (MM: 1004 g mol⁻¹) and Mn₃O₄ (MM: 228.8 g mol⁻¹) phases. Thus, the difference between the 4.9 mol % measured by WDXRF and the 4.6 mol % calculated from Rietveld refinement gives us a residue of 0.3% Mn atoms, which most likely remained in the hydroxyapatite structure after calcination. By EDS, it was possible to measure the amount of Mn remaining in the hydroxyapatite crystals in different regions relatively far from the Mn₃O₄ particles (Fig. 4). The values obtained for two different regions were 0.34-0.70%, which was slightly higher than 0.3%, most likely because of the heterogeneous distribution of Mn in the hydroxyapatite crystals, especially on the surface. Some regions experienced faster Mn diffusion, promoting the formation of large Mn₃O₄ particles. In other regions, this segregation was not complete, as evidenced by the continued presence of Mn atoms throughout the hydroxyapatite crystals.

After calcination, the absorption bands related to ${\rm CO_3}^{2-}$ in the sample containing 4.9% Mn disappeared compared to the spectrum of pure hydroxyapatite under the same conditions (Fig. 7). The insertion of Mn atoms induced the preferential occupation of ${\rm PO_4}^{3-}$ sites by ${\rm CO_3}^{2-}$, while calcination led to the complete release of ${\rm CO_3}^{2-}$ from the Mn-containing hydroxyapatite phase in the form of ${\rm CO_2}$. It seems clear that the presence of Mn atoms was responsible for this release and contributed to the decrease in lattice parameters.

The difference Fourier maps showed that the presence of Mn atoms strongly perturbed the region close to the Ca(2) sites that was responsible for forming the hexagonal OH⁻ channels in the as-synthesized samples (Fig. 8). After calcination (Fig. 9), these perturbations were much more pronounced, with the appearance of a hexagonal positive region close to the Ca(2) sites and a negative ring around the OH⁻ sites, both best observed from the 2D projection along the [0 0 1] direction. This is a strong indication of Mn atoms occupying a dislocated position in the Ca(2) sites. In particular, after calcination, the structure was much more ordered, and small lattice perturbations were more easily observed in the difference Fourier maps. Considering that a large portion of Mn atoms were segregated from the hydroxyapatite structure after 2 h of calcination, the best approach to confirm the occupation of Ca sites by Mn would be to prevent the segregation of Mn. This could further highlight the lattice perturbations caused by the presence of Mn.

Importantly, the $\rm Mn_3O_4$ nanoparticles observed on the surface of the hydroxyapatite crystals (Fig. 4) were notably formed by the diffusion of Mn atoms from the bulk toward the surface, where they could finally react with oxygen. At different temperatures, manganese oxide can assume different forms [60], as expressed in Eq. (8):

$$MnO_2 \xrightarrow{535^{\circ}C} Mn_2O_3 \xrightarrow{940^{\circ}C} Mn_3O_4$$
 (8)

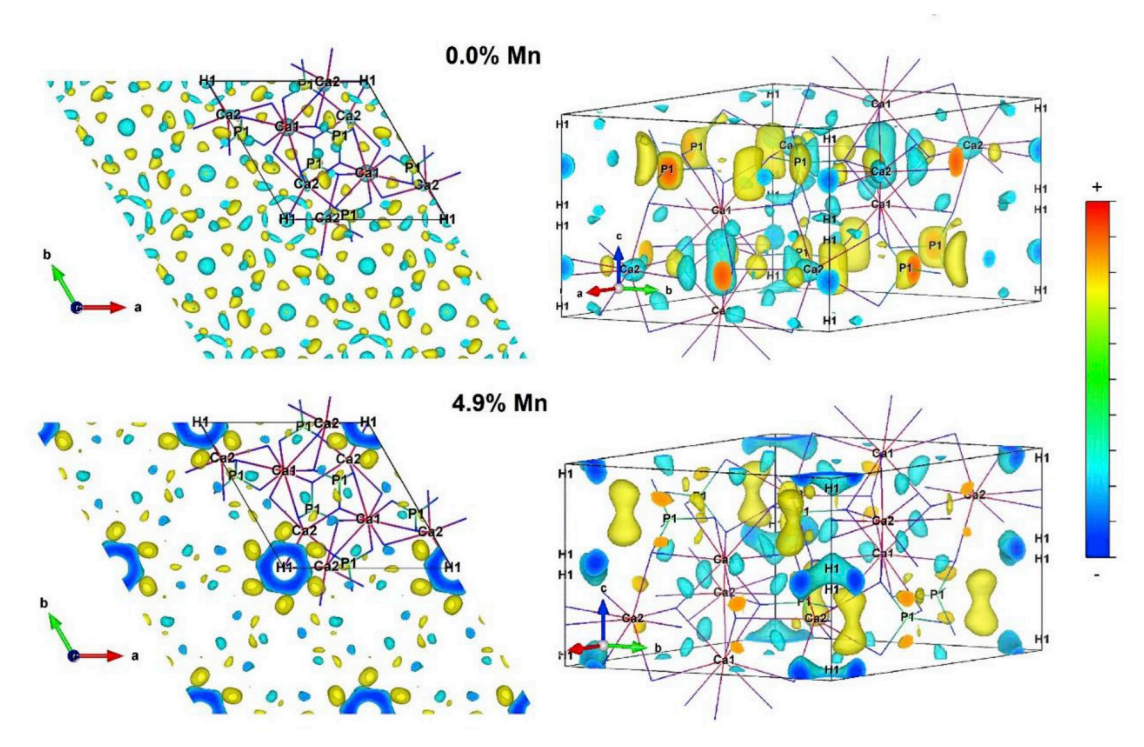


Fig. 9. 3D difference Fourier maps (F_{obs} - F_{cal}) obtained for hydroxyapatite phases containing 0.0 (Supplementary data: Fig. S12) and 4.9 (Supplementary data: Fig. S18) mol % Mn (measured by WDXRF) after calcination at 1000 °C for 2 h (heating rate of 2 °C/min). 2D images of 4 cell units of hydroxyapatite are observed along the [0 0 1] direction (left). 3D images of cell units of hydroxyapatite show in detail the perturbations around the Ca(1), Ca(2), P(1) and H(1) sites (right).

According to these reactions, thermal treatment under air at $1000\,^{\circ}\text{C}$ would produce Mn_3O_4 . In fact, this was the only manganese oxide phase observed in our calcined samples. A way to avoid the formation of this oxide, *i.e.*, the segregation of Mn atoms from the Mn-containing hydroxyapatite, was to calcine the samples at a temperature lower than 940 °C and to use a shorter calcination time to prevent diffusion. Thus, the hydroxyapatite containing 4.9 mol % Mn was also calcined at 400, 600, 800 °C and 1000 °C for only 5 min, instead the 2 h employed before, at the same heating rate (2 °C/min).

The obtained difference Fourier maps showed that the negative scattering observed at the Ca(1) sites became positive with increasing temperature (Fig. 10). At 800 °C, a small amount of Ca atoms were released from the hydroxyapatite structure in the form of CaO, but no Mn₃O₄ was formed, which means that all 4.9 mol % Mn was inserted into the crystalline hydroxyapatite lattice. At this temperature, positive perturbations were observed around Ca(2), P(1) and Ca(1) sites. After 5 min at 1000 °C, the crystallinity increased even more, and some Mn atoms began to segregate, generating 1.8 wt% Mn₃O₄, which means that approximately 2.6 mol % of the Mn atoms remained in the hydroxyapatite phase. Under this condition (1000 °C/5 min), Ca(1) sites become much more positive, effectively suggesting their occupation by the remaining Mn atoms. This seems to indicate that for a highly ordered hydroxyapatite free of CO₃²⁻, Mn atoms have a preference for Ca (1) sites, as previously observed by Suitch et al. [55] in fluorapatites heat treated at 900 °C.

The color of the sample containing 4.9% Mn changed from greengray before calcination to dark brown after calcination at 1000 °C. This color change could be directly associated with the segregation of $\rm Mn_3O_4$. However, color changes were also verified for the samples calcined at 800 °C (without the presence of $\rm Mn_3O_4$). In these cases, a dark-gray color was observed, indicating the reduction of the blue/green oxo Mn(V) species [26,61] without the formation of $\rm Mn_3O_4$.

Indeed, the XPS results demonstrated that at 800 °C, the area under the Mn(III) curve slightly increased, while the area associated with Mn(IV) decreased. As discussed above, this region is also associated with the high binding energies of MnO₄ⁿ⁻ species. By observing the difference Fourier maps obtained for the samples calcined for 5 min at 800 and 1000 °C (Fig. 10), it is possible to see a very strong positive perturbation around P(1) sites, with positive lobes between the oxygens forming the PO₄³⁻ tetrahedra. Lachwa et al. [58] have shown that MnO₄³⁻ tetrahedra can adapt to vanadate and arsenate sites of chlorapatites under isomorphic conditions. However, when replacing PO₄³⁻, MnO₄³⁻ acquires a different spatial orientation due to the larger ionic radius of Mn (V) than that of P(V). Therefore, the positive regions between the oxygens of PO₄³⁻ sites could represent the occupation of PO₄³⁻ sites by MnO₄³⁻ ions displaying a different orientation. However, these differences could also indicate the gradual reduction of MnO₄³⁻ ions, which would further perturb the region around the PO₄³⁻ sites. At the same time, the reduction of $MnO_4^{\ 3-}$ ions can produce Mn^{3+} ions, which can easily migrate to the adjacent Ca(1) positions under the effect of high temperature. The shortage of MnO₄³⁻ ions along with the release of CO₃²⁻ ions occurring at approximately 800 °C [24] will increase the Ca/P ratio, explaining why some of the Ca²⁺ ions are released in the form of CaO.

It has been assumed that $\mathrm{CO_3}^{2-}$ ions located in B-type sites must be transferred to A-type sites before being released as $\mathrm{CO_2}$ from the apatite structure during calcination [24,62,63]. In A-type sites, $\mathrm{CO_3}^{2-}$ ions can react with oxidant molecules to form gaseous $\mathrm{CO_2}$, which is released through the $\mathrm{OH^-}$ hexagonal channels [24]. This process will generate more hydroxyl vacancies (V_{OH}) in the hydroxyapatite phase, which is in accordance with the reduction in $\mathrm{OH^-}$ absorption bands observed by FTIR (Fig. 7) and the appearance of very negative scattering residues around $\mathrm{OH^-}$ groups, as seen by the difference Fourier maps (Fig. 9).

As time progressed, i.e., until 2 h at 1000 °C, the perturbation

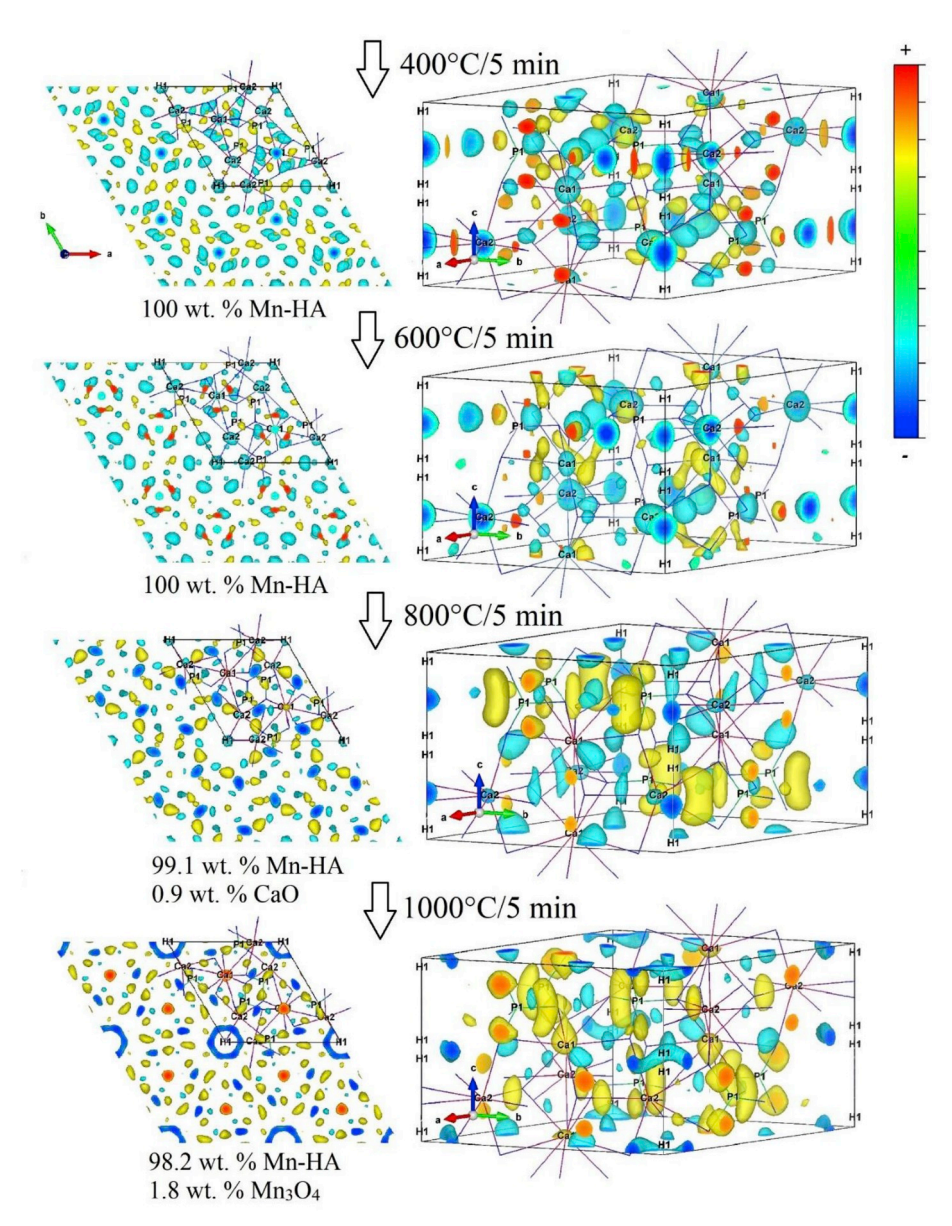


Fig. 10. 3D difference Fourier maps $(F_{obs} - F_{cal})$ obtained for the hydroxyapatite phase containing 4.9 mol % Mn (measured by WDXRF) after calcination for 5 min at 400 (Supplementary data: Figs. S14) and 600 (Supplementary data: Figs. S15) and 800 (Supplementary data: Fig. S16), and 1000 °C (Supplementary data: Fig. S17) with a heating rate of 2 °C/min 2D images of 4 cell units of hydroxyapatite are observed along the [0 0 1] direction (left). 3D images of cell units of hydroxyapatite show in detail the perturbations around the Ca(1), Ca(2), P(1) and H(1) sites (right).

around P(1) sites was significantly reduced (Fig. 9), and Ca(1) sites were no longer perturbed; then, a strong positive perturbation appeared close to the Ca(2) sites. Manganese atoms must diffuse toward the crystal surface to be segregated in the form of Mn_3O_4 nanoparticles. Considering that the {1 0 0} faces of hydroxyapatite crystals are responsible for the majority of the hydroxyapatite surface area [57], Ca (2) sites are much more exposed to the atmosphere than Ca(1) sites. Mn^{n+} ions must gain electrons to form Mn_3O_4 , and MnO_4^{3-} must be reduced to produce Mn_3O_4 and O_2 ; both reactions occur on the crystal surface. Even CO_2 molecules must be released through the OH^- channels exposed to the surface at high temperature. In general, these channels are responsible for the majority of reactions involving gaseous molecules in apatites. Therefore, it can be assumed that the perturbations in the hydroxyl channels formed by Ca(2) sites after 2 h at 1000 °C would reflect this kinetic process, in which the segregation of Mn

through the hexagonal channels is not yet complete. Even if strong segregation was observed with the formation of large Mn_3O_4 particles in some regions, in other regions, some Mn atoms remained in Ca(2) sites as a final segregation step before forming large Mn_3O_4 particles on the hydroxyapatite surface. The relative area under the Mn $2p_{3/2}$ XPS curve related to Mn(III) becomes almost twice as high as that observed for Mn(II), which is consistent with the proportion of Mn(II):Mn(III) oxidation states expected for the Mn_3O_4 spinel structure (1:2).

As mentioned before, most of the detailed literature about the occupation of Mn in the apatite lattice is focused on fluorapatites and not hydroxyapatites. Thus, our results are very important because they demonstrate how Mn behaves in a calcium-deficient carbonated hydroxyapatite with a composition and a structure very similar to those observed in the mineral phase of bones. Depending on the composition, processing temperature and time employed, Mn atoms can be

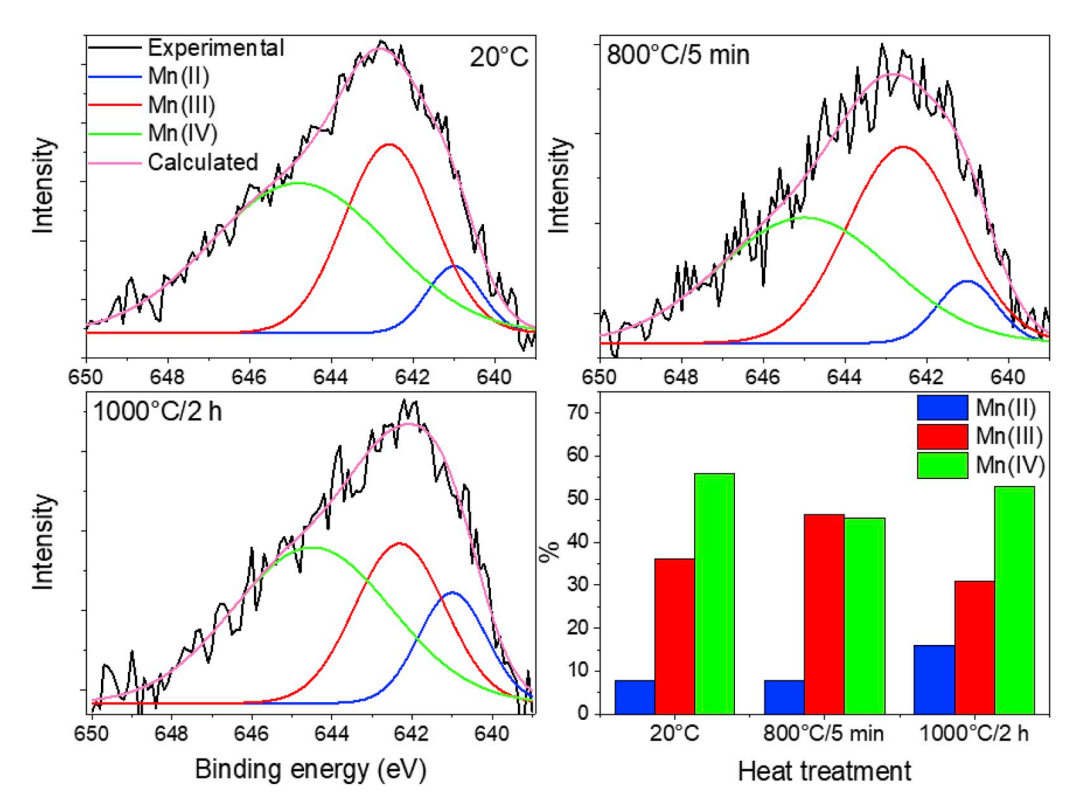


Fig. 11. Mn $2p_{3/2}$ XPS spectra and deconvoluted curves for Mn(II), Mn(III) and Mn(IV) after background subtraction of the as-synthesized sample containing 4.9 mol% Mn (20 °C) (a) and after calcination at 800 °C for 5 min (b) and 1000 °C for 2 h (c). The relative area under the deconvoluted curves associated with Mn(II), Mn(III) and Mn (IV) for each condition is shown in (d). Supplementary data can be accessed in Fig. S19.

preferentially inserted into either Ca(1) or Ca(2) sites or segregated in the form of $\rm Mn_3O_4$ nanoparticles (Supplementary data: Video S1). The amount and size of the $\rm Mn_3O_4$ nanoparticles, as well as the occupation of the hydroxyapatite sites, can directly influence the magnetic properties of the material [12,31,32]. Therefore, our findings will be fundamental for further work focused on new strategies to synthesize and process active hydroxyapatite-based scaffolds controlled by a magnetic field.

Supplementary data related to this article can be found at https://doi.org/10.1016/j.ceramint.2020.01.062.

5. Conclusions

The insertion of Mn atoms into a hydroxyapatite structure decreases its crystallinity and increases the microstrain, promoting strong thermal instability. The hydroxyapatite lattice parameters decrease with increasing Mn concentration, and the c-axis is by far the most sensitive to this decrease. In general, Mn induces several perturbations along the hydroxyl hexagonal channels, either at the OH aites or at the Ca(2) sites forming these channels. This behavior strongly indicates that Mn prefers to occupy Ca(2) sites at low temperatures, particularly when the hydroxyapatite lattice is poorly ordered and has ${\rm CO_3}^{2-}$ in a B-type position. MnO₄³⁻ ions partially replace PO₄³⁻ sites. When the temperature increases to 800°, CO₃²⁻ is released, and the structure becomes better ordered; Ca(1) sites are preferentially occupied by Mn atoms, while MnO₄³⁻ ions in PO₄³⁻ sites are reduced. Above 800 °C, Mn atoms tend to be released from the hydroxyapatite structure through the hydroxyl channels and form Mn₃O₄. In this transient condition, Mn accommodation in Ca(2) sites again becomes favorable.

Data availability

Supplementary material containing the Rietveld refinement data is accessible in the electronic version of the manuscript. Raw data will be made available upon request to the corresponding author.

Declaration of competing interest

The authors declare that they have no known competing financial interests or personal relationships that could have appeared to influence the work reported in this paper.

Acknowledgments

The authors acknowledge financial support from the Brazilian research agencies FAPITEC/SE, CAPES, and CNPq in the form of the grants PROMOB CAPES/FAPITEC-SE (Nº 88881.157913/2017–01) and PDE/CNPq (N° 205536/2018–2). The efforts of R. Shahbazian-Yassar, T. Shokuhfar, and S. Sharifi-Asl were funded by the U.S. National Science Foundation (NSF)-Biomaterials Program (BMAT) under Award N° 1710049. The authors also acknowledge LABNANO at the Brazilian Center for Research in Physics (CBPF) for the use of the JEOL JEM-2100F transmission electron microscope and the University of Illinois at Chicago (UIC). This work also made use of the JEOL JEM-ARM200CF in the Electron Microscopy Core of UIC's Research Resources Center. The acquisition of this instrument was supported by an MRI-R2 grant from the U.S. National Science Foundation (DMR-0959470).

Appendix A. Supplementary data

Supplementary data to this article can be found online at https://doi.org/10.1016/j.ceramint.2020.01.062.

References

- M. Arruebo, R. Fernández-Pacheco, M.R. Ibarra, J. Santamaría, Magnetic nanoparticles for drug delivery, Nano Today 2 (2007) 22–32, https://doi.org/10.1016/ S1748-0132(07)70084-1.
- [2] J. Huang, Y. Li, A. Orza, Q. Lu, P. Guo, L. Wang, L. Yang, H. Mao, Magnetic nanoparticle facilitated drug delivery for cancer therapy with targeted and imageguided approaches, Adv. Funct. Mater. 26 (2016) 3818–3836, https://doi.org/10. 1002/adfm.201504185.
- [3] X. Zhao, J. Kim, C.A. Cezar, N. Huebsch, K. Lee, K. Bouhadir, D.J. Mooney, Active

- scaffolds for on-demand drug and cell delivery, Proc. Natl. Acad. Sci. U. S. A 108 (2011) 67-72, https://doi.org/10.1073/pnas.1007862108.
- [4] N. Bock, A. Riminucci, C. Dionigi, A. Russo, A. Tampieri, E. Landi, V.A.A. Goranov, M. Marcacci, V. Dediu, A novel route in bone tissue engineering: magnetic biomimetic scaffolds, Acta Biomater. 6 (2010) 786–796, https://doi.org/10.1016/j.actbio.2009.09.017.
- [5] U. D'Amora, T. Russo, A. Gloria, V. Rivieccio, V. D'Antò, G. Negri, L. Ambrosio, R. De Santis, 3D additive-manufactured nanocomposite magnetic scaffolds: effect of the application mode of a time-dependent magnetic field on hMSCs behavior, Bioact. Mater. 2 (2017) 138–145, https://doi.org/10.1016/j.bioactmat.2017.04. 003.
- [6] H.-M. Yun, S.-J. Ahn, K.-R. Park, M.-J. Kim, J.-J. Kim, G.-Z. Jin, H.-W. Kim, E.-C. Kim, Magnetic nanocomposite scaffolds combined with static magnetic field in the stimulation of osteoblastic differentiation and bone formation, Biomaterials 85 (2016) 88–98, https://doi.org/10.1016/j.biomaterials.2016.01.035.
- [7] A.A. Adedoyin, A.K. Ekenseair, Biomedical applications of magneto-responsive scaffolds, Nano Res. 11 (2018) 5049–5064, https://doi.org/10.1007/s12274-018-2198-2.
- [8] S. Mondal, P. Manivasagan, S. Bharathiraja, M. Santha Moorthy, H.H. Kim, H. Seo, K.D. Lee, J. Oh, Magnetic hydroxyapatite: a promising multifunctional platform for nanomedicine application, Int. J. Nanomed. 12 (2017) 8389–8410, https://doi.org/ 10.2147/INS147355
- [9] S.V. Dorozhkin, Biphasic, triphasic, and multiphasic calcium orthophosphates, Adv. Ceram. 8 (2016) 33–95, https://doi.org/10.1002/9781119242598.ch2.
- [10] M. Šupová, Substituted hydroxyapatites for biomedical applications: a review, Ceram. Int. 41 (2015) 9203–9231, https://doi.org/10.1016/j.ceramint.2015.03. 316.
- [11] J.M. Hughes, J.F. Rakovan, Structurally robust, chemically diverse: apatite and apatite supergroup minerals, Elements 11 (2015) 165–170, https://doi.org/10. 2113/gselements.11.3.165.
- [12] A. Tampieri, T. D'Alessandro, M. Sandri, S. Sprio, E. Landi, L. Bertinetti, S. Panseri, G. Pepponi, J. Goettlicher, M. Bañobre-López, J. Rivas, T. D'Alessandro, M. Sandri, S. Sprio, E. Landi, L. Bertinetti, S. Panseri, G. Pepponi, J. Goettlicher, M. Bañobre-López, J. Rivas, Intrinsic magnetism and hyperthermia in bioactive Fe-doped hydroxyapatite, Acta Biomater. 8 (2012) 843–851, https://doi.org/10.1016/j.actbio. 2011.09.032.
- [13] W. Pon-On, S. Meejoo, I.-M.M. Tang, Substitution of manganese and iron into hydroxyapatite: core/shell nanoparticles, Mater. Res. Bull. 43 (2008) 2137–2144, https://doi.org/10.1016/j.materresbull.2007.09.004.
- [14] N. Petchsang, W. Pon-On, J.H.H. Hodak, I.M.M. Tang, Magnetic properties of Coferrite-doped hydroxyapatite nanoparticles having a core/shell structure, J. Magn. Magn. Mater. 321 (2009) 1990–1995, https://doi.org/10.1016/j.jmmm.2008.12.
- [15] P.M.C. Torres, S.I. Vieira, A.R. Cerqueira, S. Pina, O.A.B. da Cruz Silva, J.C.C. Abrantes, J.M.F. Ferreira, Effects of Mn-doping on the structure and biological properties of β-tricalcium phosphate, J. Inorg. Biochem. 136 (2014) 57–66, https://doi.org/10.1016/j.jinorgbio.2014.03.013.
- [16] M.J.J. Robles-Águila, J.A.A. Reyes-Avendaño, M.E.E. Mendoza, Structural analysis of metal-doped (Mn, Fe, Co, Ni, Cu, Zn) calcium hydroxyapatite synthetized by a sol-gel microwave-assisted method, Ceram. Int. 43 (2017) 12705–12709, https:// doi.org/10.1016/j.ceramint.2017.06.154.
- [17] W. Acchar, E.G. Ramalho, Effect of MnO2 addition on sintering behavior of tricalcium phosphate: preliminary results, Mater. Sci. Eng. C 28 (2008) 248–252, https://doi.org/10.1016/j.msec.2006.12.011.
- [18] I. Sopyan, A.N. Natasha, Preparation of nanostructured manganese-doped biphasic calcium phosphate powders via sol–gel method, Ionics 15 (2009) 735–741, https://doi.org/10.1007/s11581-009-0330-8.
- [19] S. Lala, T.N.N. Maity, M. Singha, K. Biswas, S.K.K. Pradhan, Effect of doping (Mg,Mn,Zn) on the microstructure and mechanical properties of spark plasma sintered hydroxyapatites synthesized by mechanical alloying, Ceram. Int. 43 (2017) 2389–2397, https://doi.org/10.1016/j.ceramint.2016.11.027.
- [20] E. Boanini, M. Gazzano, A. Bigi, Ionic substitutions in calcium phosphates synthesized at low temperature, Acta Biomater. 6 (2010) 1882–1894, https://doi.org/10. 1016/j.actbio.2009.12.041.
- [21] B. Bracci, P. Torricelli, S. Panzavolta, E. Boanini, R. Giardino, A. Bigi, Effect of Mg2+, Sr2+, and Mn2+ on the chemico-physical and in vitro biological properties of calcium phosphate biomimetic coatings, J. Inorg. Biochem. 103 (2009) 1666–1674, https://doi.org/10.1016/j.jinorgbio.2009.09.009.
- [22] L. Yu, Y. Tian, Y. Qiao, X. Liu, Mn-containing titanium surface with favorable osteogenic and antimicrobial functions synthesized by PIII&D, Colloids Surfaces B Biointerfaces 152 (2017) 376–384, https://doi.org/10.1016/j.colsurfb.2017.01.047.
- [23] L. Yu, S. Qian, Y. Qiao, X. Liu, Multifunctional Mn-containing titania coatings with enhanced corrosion resistance, osteogenesis and antibacterial activity, J. Mater. Chem. B. 2 (2014) 5397, https://doi.org/10.1039/C4TB00594E.
- [24] M. Pereira, G. Dulce, D.A. Soares, J. Dentzer, K. Anselme, L. Ágata, D. Sena, A. Kuznetsov, E. Araujo, M.P. Moreira, G.D. de Almeida Soares, J. Dentzer, K. Anselme, L.Á. de Sena, A. Kuznetsov, E.A. dos Santos, Synthesis of magnesiumand manganese-doped hydroxyapatite structures assisted by the simultaneous incorporation of strontium, Mater. Sci. Eng. C 61 (2016) 736–743, https://doi.org/ 10.1016/j.msec.2016.01.004.
- [25] G. Renaudin, S. Gomes, J.-M.M. Nedelec, First-row transition metal doping in calcium phosphate bioceramics: a detailed crystallographic study, Materials 10 (2017) 92, https://doi.org/10.3390/ma10010092.
- [26] C. Paluszkiewicz, A. Ślósarczyk, D. Pijocha, M. Sitarz, M. Bućko, A. Zima, A. Chróścicka, M. Lewandowska-Szumieł, Synthesis, structural properties and

- thermal stability of Mn-doped hydroxyapatite, J. Mol. Struct. 976 (2010) 301–309, https://doi.org/10.1016/j.molstruc.2010.04.001.
- [27] I. Mayer, O. Jacobsohn, T. Niazov, J. Werckmann, M. Iliescu, M. Richard-Plouet, O. Burghaus, D. Reinen, Manganese in precipitated hydroxyapatites, Eur. J. Inorg. Chem. (2003) 1445–1451, https://doi.org/10.1002/ejic.200390188 2003.
- [28] J. Hem, Chemical equilibria and rates of manganese oxidation chemistry of manganese in natural water, US Geol. Surv. Water Supply Pap. 1667 (1963) 71 Paper 1667-A.
- [29] L. Narayani, V. Jagadeesha Angadi, A. Sukhdev, M. Challa, S. Matteppanavar, P.R.R. Deepthi, P. Mohan Kumar, M. Pasha, Mechanism of high temperature induced phase transformation and magnetic properties of Mn 3 O 4 crystallites, J. Magn. Magn. Mater. 476 (2019) 268–273, https://doi.org/10.1016/j.jmmm.2018. 12 072
- [30] M. Kluenker, M.N. Tahir, R. Dören, M. Deuker, P. Komforth, S. Plana-Ruiz, B. Barton, S.I. Shylin, V. Ksenofontov, M. Panthöfer, N. Wiesmann, J. Herzberger, A. Möller, H. Frey, J. Brieger, U. Kolb, W. Tremel, Iron oxide superparticles with enhanced MRI performance by solution phase epitaxial growth, Chem. Mater. 30 (2018) 4277–4288, https://doi.org/10.1021/acs.chemmater.8b01128.
- [31] M.E. Zilm, L. Yu, W.A. Hines, M. Wei, Magnetic properties and cytocompatibility of transition-metal-incorporated hydroxyapatite, Mater. Sci. Eng. C 87 (2018) 112–119, https://doi.org/10.1016/j.msec.2018.02.018.
- [32] A. Kyriacou, B.C. Chakoumakos, V.O. Garlea, A.J. Rondinone, K.D. Sorge, Combined X-Ray and Neutron Diffraction Rietveld Refinement in Iron-Substituted Nano-Hydroxyapatite, (2013), pp. 3535–3545, https://doi.org/10.1007/s10853-013-7148-5.
- [33] J. Rodríguez-Carvajal, Recent advances in magnetic structure determination by neutron powder diffraction, Phys. B Condens. Matter 192 (1993) 55–69, https://doi.org/10.1016/0921-4526(93)90108-I.
- [34] K. Momma, F. Izumi, VESTA: a three-dimensional visualization system for electronic and structural analysis, J. Appl. Crystallogr. 41 (2008) 653–658, https://doi.org/10.1107/s0021889808012016.
- [35] D. Eichert, C. Drouet, H. Sfihi, C. Rey, C. Combes, Nanocrystalline Apatite-Based Biomaterials, UK ed., Nova Science Publishers, Inc., New York, 2009.
- [36] C. Zhang, J. Lan, S. Wang, S. Han, H. Yang, Q. Niu, J. Wang, Q. Wang, Y. Xiang, Y. Wu, X. Zhang, H. Lin, X. Zhang, H. Qiao, Y. Huang, Silver nanowires on acidalkali-treated titanium surface: bacterial attachment and osteogenic activity, Ceram. Int. 45 (2019) 24528–24537, https://doi.org/10.1016/j.ceramint.2019.08.
- [37] H. Qiao, C. Zhang, X. Dang, H. Yang, Y. Wang, Y. Chen, L. Ma, S. Han, H. Lin, X. Zhang, J. Lan, Y. Huang, Gallium loading into a polydopamine-functionalised SrTiO3 nanotube with combined osteoinductive and antimicrobial activities, Ceram. Int. 45 (2019) 22183–22195, https://doi.org/10.1016/j.ceramint.2019.07. 240.
- [38] Q. Zou, Y. Wei, W. Zhang, X. Guo, X. Liu, A. Xu, X. Li, X. Ruan, Synergistic activation of peroxymonosulfate for organic pollutants degradation with hydroxyapatite/manganese oxides hybrid catalysts, Appl. Surf. Sci. 501 (2020) 144322, https://doi.org/10.1016/j.apsusc.2019.144322.
- [39] Z. Huang, W. Zhou, C. Ouyang, J. Wu, F. Zhang, J. Huang, Y. Gao, J. Chu, High performance of Mn-Co-Ni-O spinel nanofilms sputtered from acetate precursors, Sci. Rep. 5 (2015) 10899, https://doi.org/10.1038/srep10899.
- [40] J. Töpfer, A. Feltz, D. Gräf, B. Hackl, L. Raupach, P. Weissbrodt, Cation valencies and distribution in the spinels NiMn2O4 and MzNiMn2 – zO4 (M = Li, Cu) studied by XPS, Phys. Status Solidi 134 (1992) 405–415, https://doi.org/10.1002/pssa. 2211340211.
- [41] W.P. Kilroy, S. Dallek, J. Zaykoski, Synthesis and characterization of metastable Li–Mn–O spinels from Mn(V), J. Power Sources 105 (2002) 75–81, https://doi.org/ 10.1016/S0378-7753(01)00973-9.
- [42] M. Mosiałek, G. Mordarski, P. Nowak, W. Simka, G. Nawrat, M. Hanke, R.P. Socha, J. Michalska, Phosphate-permanganate conversion coatings on the AZ81 magnesium alloy: SEM, EIS and XPS studies, Surf. Coat. Technol. 206 (2011) 51–62, https://doi.org/10.1016/j.surfcoat.2011.06.035.
- [43] E.A.P. De Maeyer, R.M.H. Verbeeck, D.E. Naessens, Optimalization of the preparation of Na+- and CO2-3-containing hydroxyapatite by the hydrolysis of monetite, J. Cryst. Growth 135 (1994) 539–547, https://doi.org/10.1016/0022-0248(94)90145-7.
- [44] N.H. De Leeuw, J.R. Bowe, J.A.L.L. Rabone, A computational investigation of stoichiometric and calcium-deficient oxy- and hydroxy-apatites, Faraday Discuss 134 (2007) 195–214, https://doi.org/10.1039/b602012g.
- [45] F.A. Kröger, H.J. Vink, Relations between the Concentrations of Imperfections in Crystalline Solids, (1956), pp. 307–435, https://doi.org/10.1016/S0081-1947(08) 60135-6.
- [46] F. Borba, L. Melo, T. Oliveira, L. Eduardo, F.B. Simões, L.M. da Silva, T.O. Fonseca, L.E. Almeida, E.A. dos Santos, Isolated effects of microwave radiation on the solid-liquid interface reactions between hydroxyapatite nanocrystals and silver ions, Ceram. Int. 44 (2018) 16960–16971, https://doi.org/10.1016/j.ceramint.2018.06.
- [47] S.V. Dorozhkin, Calcium orthophosphates in nature, biology and medicine, Materials 2 (2009) 399–498, https://doi.org/10.3390/ma2020399.
- [48] C. Ortali, I. Julien, M. Vandenhende, C. Drouet, E. Champion, Consolidation of bone-like apatite bioceramics by spark plasma sintering of amorphous carbonated calcium phosphate at very low temperature, J. Eur. Ceram. Soc. 38 (2018) 2098–2109, https://doi.org/10.1016/j.jeurceramsoc.2017.11.051.
- [49] J.C. Elliott, Calcium phosphate biominerals, phosphates geochemical, Geobiol. Mater. Importance 48 (2019) 427–453, https://doi.org/10.2138/rmg.2002.48.11.
- [50] R.Z. Leors, M.H. Taheri, G.B. Quirologico, J.P. Legeros, Formation and stability of apatites: effects of some cationic substituents, Second Int. Congr. Phosphorus

- Compd., Boston, 1980, pp. 89-103.
- [51] I. Mayer, F.J.G. Cuisinier, I. Popov, Y. Schleich, S. Gdalya, O. Burghaus, D. Reinen, Phase relations between β-tricalcium phosphate and hydroxyapatite with manganese(II): structural and spectroscopic properties, Eur. J. Inorg. Chem. (2006) 1460–1465, https://doi.org/10.1002/ejic.200501009 2006.
- [52] K. Kandori, Y. Yamaguchi, Synthesis and characterization of Mn-doped calcium hydroxyapatite particles, Phosphorus Res. Bull. 33 (2017) 26–34, https://doi.org/ 10.3363/prb.33.26.
- [53] K. Kandori, R. Murata, Y. Yamaguchi, A. Yoshioka, Protein adsorption behaviors onto Mn(II)-doped calcium hydroxyapatite particles with different morphologies, Colloids Surfaces B Biointerfaces 167 (2018) 36–43, https://doi.org/10.1016/j. colsurfb.2018.03.043.
- [54] Y. Li, J. Widodo, S. Lim, C.P. Ooi, Synthesis and cytocompatibility of manganese (II) and iron (III) substituted hydroxyapatite nanoparticles, J. Mater. Sci. 47 (2012) 754–763, https://doi.org/10.1007/s10853-011-5851-7.
- [55] P.R. Suitch, J.L. LaCout, A. Hewat, R.A. Young, The structural location and role of Mn 2+ partially substituted for Ca 2+ in fluorapatite, Acta Crystallogr. Sect. B Struct. Sci. 41 (1985) 173–179, https://doi.org/10.1107/S0108768185001896.
- [56] J.M. Hughes, M. Cameron, K.D. Crowley, Ordering of divalent cations in the apatite structure: crystal structure refinements of natural Mn- and Sr-bearing apatite, Am. Mineral. 76 (1991) 1857–1862.

- [57] J.C. Elliott, Structure and Chemistry of the Apatites and Other Calcium Orthophosphates, ELSEVIER, London, UK, 1994.
- [58] H. Lachwa, D. Reinen, Color and electronic structure of manganese(V) and manganese(VI) in tetrahedral oxo coordination. A spectroscopic investigation, Inorg. Chem. 28 (1989) 1044–1053, https://doi.org/10.1021/ic00305a011.
- [59] J.D. Kingsley, J.S. Prener, B. Segall, Spectroscopy of MnO43- in calcium halophosphates, Phys. Rev. 137 (1965) A189–A202, https://doi.org/10.1103/PhysRev.137. A189.
- [60] J.A.K. Tareen, B. Basavalingu, G.T. Bhandage, T.R.N. Kutty, Hydrothermal stability of some manganese oxides, Bull. Mater. Sci. 10 (1988) 199–203, https://doi.org/ 10.1007/BF02744064.
- [61] Y. Li, C.P.A.T. Klein, X. Zhang, K. de Groot, Relationship between the colour change of hydroxyapatite and the trace element manganese, Biomaterials 14 (1993) 969–972, https://doi.org/10.1016/0142-9612(93)90187-7.
- [62] H. El Feki, I. Khattech, M. Jemal, C. Rey, Thermal decomposition of carbonated containing sodium ions, Thermochim. Acta 237 (1994) 99–110.
- [63] J. Shi, A. Klocke, M. Zhang, U. Bismayer, Thermallly-induced structural modification of dental enamel apatite: decomposition and transformation of carbonate groups, Eur. J. Mineral. 17 (2005) 769–775, https://doi.org/10.1127/0935-1221/ 2005/0017-0769.